Experimental study on the response of thin aluminium and steel plates subjected to airblast loading

V. Aune[a,*], E. Fagerholt[a], K.O. Hauge[b], M. Langseth[a] and T. Børvik[a]

[a] Structural Impact Laboratory (SIMLab) and Centre for Advanced Structural Analysis (CASA), Department of Structural Engineering, Norwegian University of Science and Technology, NO-7491 Trondheim, Norway

[b] Norwegian Defence Estates Agency, Research and Development Section, NO-0103 Oslo, Norway

Abstract

This work presents results from an experimental investigation on the influence of stand-off distance on the dynamic response of thin ductile plates subjected to airblast loading. The square plates had an exposed area of 0.3×0.3 m^2 and were manufactured from two different materials, i.e., medium-strength steel and low-strength aluminium. The airblast loading was generated by detonating spherical charges of plastic explosive at various stand-off distances relative to the centre of the plates. Piezoelectric pressure sensors were used for pressure recordings, and synchronized with two high-speed cameras in a stereoscopic setup to capture the response of the targets. The 0.8 mm thick plates were painted with a speckle pattern to measure the transient deformation fields using a three-dimensional digital image correlation (3D-DIC) technique. The tests covered the entire range of structural response from complete failure at the support to a more counter-intuitive behaviour where the permanent mid-point deflection was in the opposite direction to the incident blast wave due to reversed snap buckling. The synchronization of the pressure and displacement measurements enabled a thorough examination of the entire experiment. The trend in all tests was that the maximum response is driven by the positive impulse from the airblast, as it occurred after the positive duration of the pressure pulse. However, depending on the intensity of the blast load and the structural characteristics, elastic effects and the negative phase could play an important role in the final configuration of the plate. Comparison of the permanent deflection and the measurements from digital image correlation confirmed that this technique is capable of accurately measuring the structural response at high loading rates.

Keywords: Airblast loading; ductile plates; pressure measurements; 3D-DIC; elasto-plastic dynamic response

* Corresponding author. Tel.: + 47-73-59-47-05.

E-mail address: vegard.aune@ntnu.no (V. Aune).

1. Introduction

Protection of industrial, military and civilian engineering structures against blast loading has received a lot of attention in recent years (see e.g. Hanssen et al. [1] and Børvik et al. [2][3]). Such structures are often made of steel or aluminium plates. Steel is often preferred due to its combination of high strength, high ductility and good formability, resulting in an effective load carrying capability at a relatively low cost compared to many other materials. During the last decades aluminium alloys have become increasingly more attractive for structural applications, particularly due to its relatively high strength to weight ratio. Since thin plates are frequently being used in engineering structures, it has become necessary to evaluate the structural response of such components exposed to blast loading.

Nurick and Martin [4][5] presented a comprehensive literature review of thin plates subjected to blast loading. These studies included theoretical considerations, experimental techniques and experimental results for relatively large permanent displacements. Nurick and Martin [5] also suggested a non-dimensional empirical analysis in an attempt to compare experimental results from various studies using different loading parameters, plate dimensions and materials. This approach has proven to be a useful guideline to predict the maximum deflection of impulsively loaded plates.

Menkes and Opat [6] reported failure modes on clamped aluminium beams subjected to blast loading using sheet explosives. By monotonically increasing the impulse they identified three different damage modes, i.e., large inelastic deformation (mode I), tensile tearing at supports (mode II) and transverse shear at supports (mode III). Teeling-Smith and Nurick [7] found the same failure modes for clamped circular plates subjected to impulsive loading, and reported that the magnitude and shape of the deformed plates depend on the intensity of the loading. These failure modes were also observed for blast loaded square plates by Olson et al. [8]. However, a slight change in the interpretation was needed to account for tensile tearing at

the supports as failure was first observed at the centre of the boundary before progressing towards the corners with increasing impulse. Subsequent work by Nurick et al. [9][10] extended these failure modes by including necking at the boundary for mode I, and some geometric additions to mode II by including the amount of tearing at the boundary (called mode II* in the literature). Thus, experimental evidence was used to show a significant effect of the boundary conditions when predicting tearing. Similar results were also reported by Wierzbicki and Nurick [11].

The dynamic elasto-plastic structural response under pulse loading may be divided into three categories depending on the intensity of the loading and the permanent mid-point deflection (see e.g. [12][13]). If the structural component oscillates on both sides of its original configuration with a positive final deflection this is called Type I. However, if the pulse is more intense the structural component will oscillate only on the positive side of the original configuration (Type II). Finally, the structural component may first deform in the positive direction and then rebound to the negative side of the original configuration (Type III). The two first types of response are intuitive as the final deflection is positive (i.e., in the same direction as the external loading), while the latter type confounds intuition as the final deflection is negative (i.e., in the direction opposite to the external loading). This phenomenon was first reported during numerical studies by Symonds and Yu [14] and called counter-intuitive behaviour (CIB). They noted that this behaviour was extremely sensitive to the structural and loading parameters, and concluded that the response pattern was strongly dependent on the peak deflection or the release angle at which reverse motion starts. That is, CIB only occurred within some narrow range of structural and loading conditions during the transition from elastic to moderate plastic deformations, and that this behaviour could be related to the phenomenon of reversed snap buckling. The unexpected nature of this behaviour has received much attention during the years [15][16][17], and is still a topic of

interest in the literature [18]. Theoretical and numerical investigations have managed to associate the phenomenon with chaotic and complex vibrations [17][19], and this insight has motivated experiments to confirm both theoretical and numerical investigations [13][20][21].

Today's research on structural response of plates exposed to airblast loading is often based on the ballistic pendulum approach using a sheet explosive (e.g. [22][23][24]), or free airblast experiments using an explosive charge at a given stand-off distance from the plate (e.g. [25][26][27]). All setups are in general interested in the permanent deflection and deformed shape of the plate. However, due to the complex nature of an explosion the experimental results are evaluated using various methods. Some data are compared to analytical and empirical methods, as those presented by Nurick and Martin [4], while other results are used to validate numerical methods' ability to describe both the loading and the structural response [26][28][29].

Measurement techniques are equally important as the experimental setup since they determine the usefulness, reliability and validity of the experimental data. Until recently it was difficult to measure the deflection-time history of plates exposed to blast loading. However, the recent development of three-dimensional digital image correlation (3D-DIC) techniques has enabled such measurements of the complete deformation history during blast experiments [27][28][30][31]. The two most common techniques are the subset-based local DIC [32] and the finite element-based global DIC [33]. Tiwari et al. [30] and Zhao et al. [31] used subset-based local 3D-DIC to obtain full-field transient deformations of thin aluminium plates during buried blast events to simulate realistic ground conditions and to validate a dimensional analysis, respectively. Spranghers et al. [27][28] used a similar subset-based DIC technique for full-field measurements of aluminium plates under free airblast loading conditions.

4

The objective of the present study is to investigate the dynamic response of thin ductile plates by performing controllable small-scale airblast experiments. The square plates with dimensions 0.4×0.4 m^2 were made of 0.8 mm thick Docol 600 DL steel and EN AW 1050A-H14 aluminium sheets. The loading, and consequently the structural response, was varied by positioning the explosive charge of C-4 at various stand-off distances relative to the centre point of the plates. Piezoelectric pressure sensors were used for pressure recordings and synchronized with two high-speed cameras to capture the structural response using a finite element-based 3D-DIC technique. Material tests were also performed to determine the materials' behaviour at large plastic strains. The experimental results provide a set of data which can be used to validate the reliability, robustness and effectiveness of available computational methods in predicting the structural response of thin ductile plates exposed to blast loading.

2. Experimental study

2.1. Experimental setup and programme

All experiments were performed at an indoor test facility possessed by the Research and Development Section at the Norwegian Defence Estates Agency. The experimental setup is shown in Figure 1(a) and 1(b) and was inspired by Spranghers et al. [27]. The setup consisted of a steel mounting frame fixed to the concrete floor with outer dimensions 1.0 m$\times 1.0$ m$\times 0.015$ m and a square opening of 0.3 m$\times 0.3$ m in the centre. The square plate specimens with dimensions of 0.4 m$\times 0.4$ m$\times 0.0008$ m were clamped to the rigid frame using bolted connections and a clamping frame in an attempt to achieve fixed boundary conditions. The 16 bolts were tightened using a wrench with a torque M_t of 200 Nm, which is equivalent to a preloading force F_p of 92.6 kN [34] for the M12 bolts used in this study.

Two high-speed cameras in a stereoscopic setup were used to capture the response of the

thin plates with a framing rate of 21,000 fps. The plates were painted with a speckle pattern to

measure the transient deformation fields using a 3D-DIC technique (Figure 1(c)). It was

necessary with additional lighting for the speckle pattern to have enough contrast to calculate

the transient deformation fields using DIC. The cameras were triggered manually and the

trigger mode was centred such that an equal number of frames before and after the explosion

were stored. A blast pencil was used to determine when the shock wave arrived at the cameras

(Figure 1(a) and 1(b)). From this point on the correlation of the images had reduced accuracy

due to possible oscillations of the cameras, resulting in a loss of calibration of the system.

The explosive mass W was positioned at various stand-off distances R relative to the

centre point of the plate depending on the material, and the test matrix is given in Table 1.

The explosive material was Composition C-4 with a spherical shape, a mass of 30 g

(equivalent to 40.2 g of TNT) and a diameter of approximately 34.5 mm. The blast was

initiated by an electric detonator of type RP-83 exploding bridgewire (EBW) with a TNT

equivalent of 1 g. The explosive charge and detonator were held together using a black

electrical insulation tape (Figure 1(d)).

Piezoelectric pressure sensors (Kistler 603B), corresponding charge amplifiers (Kistler

5064) and data acquisition systems from National Instruments (NI USB-6356) and Yokogawa

(DL850E ScopeCorder) were used to measure the pressure at various locations during the

experiments (see Figure 1(c) and 1(e)). These sensors are designed to measure fluctuations of

high frequency with short rise time, and are capable of measuring pressures up to 200 bar at

temperatures up to 200$^{\text{o}}$C [35]. The pressure transducers were positioned in threaded adapters

which were fastened at the desirable locations. The pressure was recorded using two

independently operating acquisition systems and sampling frequencies, i.e., 10 MHz and 21

kHz. The first frequency enabled the recording of the steep gradient and short rise time of the

blast wave, while the second frequency was the same as for the high-speed cameras enabling a synchronization of the pressure and the 3D-DIC measurements. No low-pass filtering was used in the pressure measurements.

Before testing the thin steel and aluminium plates against blast loading, similar tests were performed on a massive steel plate with a thickness of 15 mm. The main objective with these experiments was to investigate the pressure distribution on a rigid calibration plate, and to use these measurements as a basis to investigate potential fluid-structure interaction (FSI) effects in the thin-plate tests. To enable the investigation of the FSI effects the clamping frame had to be positioned at the same location for both the pressure measurements and the subsequent thin-plate tests. The calibration plate was therefore placed on the same side as the high-speed cameras, i.e., on the opposite side of the steel mounting frame compared to the clamping frame (see Figure 1(a)). This resulted in a slightly different stand-off distance for the loading of the calibration plate compared to the steel and aluminium plates (Figure 1(c) and 1(e)).

The calibration tests were performed using three different stand-off distances and with a sufficient amount of pressure transducers to determine the pressure distribution along the vertical and diagonal of the calibration plate. The position of the 10 pressure transducers used in these tests are shown in Figure 2(a). To reduce the risk of damaging the pressure sensors, the calibration tests were not performed at a stand-off distance of 0.125 m (see Table 1). Transducers 1-4 and 8-10 were mounted on the calibration plate, while 5-7 were located on the clamping frame. Transducer 1 was moved to the remaining position (lower centre part) in the clamping frame for the thin-plate experiments and renamed sensor 11 (Figure 2(b)). A break wire was used to determine the time of detonation which was synchronized with the pressure measurements. This is an analog device with an electric circuit which registers the time of a potential break in the wire as a change in the signal. As soon as the explosive charge detonates, the wire will break and thus define the time of detonation.

7

2.2. Materials

The 0.8 mm thick steel plates used in these tests were manufactured from medium-strength, high-hardening and cold-rolled sheets of type Docol 600DL produced by Swedish Steel Ltd. (SSAB). The steel is subjected to a heat treatment which results in a two-phase structure of ferrite and martensite, where the ferrite gives the forming properties and the martensite gives the strength. This material is often used in the automotive industry. Table 2 gives the nominal chemical composition of the material [36]. The nominal yield stress was reported by the manufacturer to be in the range from 280 MPa to 360 MPa, while the nominal tensile strength was stated to be between 600 MPa and 700 MPa.

Gruben et al. [37] investigated the mechanical properties of Docol 600DL steel by performing a comprehensive experimental study on 2 mm thick plates, while Rakvåg et al. [38] and Holmen et al. [39] performed material tests on respectively 0.7 mm and 0.8 mm thick plates of the same material. These studies compared the material behaviour in three different directions ($0°, 45°, 90°$) regarding the rolling direction of the plate, and concluded that the material is isotropic with a small variation in failure strain. The material was also found to be moderately strain rate sensitive at elevated strain rates [38]. It should further be noted that the material specimens used by Holmen et al. [39] were taken from the same plates as those used in this study. Thus, the material data provided in [39] also apply in this study, and no additional material tests were performed for the steel.

The 0.8 mm thick aluminium plates were manufactured from low-strength, strain-hardened and cold-rolled sheets of the alloy EN AW 1050A-H14 produced by Norsk Hydro ASA. This is 99.5% pure aluminium subjected to annealing before work hardened by rolling until a yield stress which is approximately half of the ultimate tensile strength is achieved. The material is often used for sheet work where high mechanical properties are not required. The nominal chemical composition is provided in Table 3, while the nominal yield and

8

ultimate tensile strengths were given by the producer to be 75 MPa and 105-145 MPa, respectively.

Uniaxial tensile tests were carried out on dog-bone specimens cut from the aluminium plates using the same geometry as in [39]. The tests were performed in a Zwick/Roell Z030 testing machine at a constant deformation rate of 2.1 mm/min. This corresponds to an initial strain rate of $\dot{\varepsilon} = 5 \times 10^{-4}$ s^{-1} for a gauge length of 70 mm. Three parallel tests were performed in three different directions ($0°, 45°, 90°$) with respect to the rolling direction of the plate. The force and displacement were measured by the hydraulic test machine at 4 Hz for all tests, and the displacement field was measured using DIC. In addition, the first test in each series was instrumented with an extensometer to measure the displacement of the gauge length for comparison with the DIC measurements. The DIC measurements were validated by using a vector at the same location and of the same length as the extensometer. The DIC measurements and the extensometer showed excellent agreement, and only the DIC recordings are therefore used in the following.

Nominal stress-strain curves from quasi-static uniaxial tensile tests of both materials are shown in Figure 3. It is observed that the aluminium is slightly anisotropic both in flow stress and failure strain (Figure 3(b)). Diffuse necking occurs at very small plastic strains (approximately 0.7%) in all three directions, which indicates that the deformation before necking is very low for this alloy. This can be explained by the manufacturing process since these sheets were formed and work-hardened by cold-rolling until half hard, i.e., to a yield stress approximately half the ultimate tensile strength [40]. It is well known that increasing the yield stress by cold-working will reduce the ductility before necking.

Following the same procedure as Holmen et al. [39], the parameters for the aluminium material was calibrated against the DIC measurements. Thus, the material behaviour is described according to a thermoelastic-thermoviscoplastic constitutive relation proposed by

Børvik et al. [41], which is implemented as *MAT_107* in LS-DYNA [42]. This model accounts for large plastic strains, high strain rates and possible temperature softening, and may be used in future numerical simulations to capture the blast response of the plates. The constitutive equation reads

$$\sigma_{eq} = \left[\sigma_0 + \sum_{i=1}^{2} Q_i \left(1 - \exp\left(-C_i p\right)\right) \right] \left[1 + \dot{p}^*\right]^c \left[1 - T^{*m}\right] \tag{1}$$

where σ_{eq} is the equivalent von Mises stress, p is the equivalent plastic strain, σ_0 represents the yield stress and (Q_i, C_i, c, m) are material constants. The dimensionless plastic strain rate is given by $\dot{p}^* = \dot{p} / \dot{p}_0$, where $\dot{p}_0$ is a user-defined reference strain rate. The homologous temperature is defined as $T^* = (T - T_r)/(T_m - T_r)$, where T is the absolute temperature, T_r is the ambient temperature and T_m is the melting temperature of the material. The first term in Eq. (1) represents the extended Voce hardening rule and was chosen due to its capability of capturing the observed rapid stagnation in the strain hardening, since this hardening rule approaches an asymptotic stress for large plastic strains. If required, the temperature change due to adiabatic heating can be calculated as

$$\Delta T = \int_0^p \chi \frac{\sigma_{eq} dp}{\rho C_p} \tag{2}$$

where ρ is the material density, C_p is the specific heat and χ is the Taylor-Quinney coefficient that represents the proportion of plastic work converted into heat.

The material parameters (σ_0, Q_i, C_i) were obtained by inverse modelling using a finite element (FE) model of the material test specimen in LS-DYNA and the optimization package LS-OPT [42]. LS-OPT reads LS-DYNA input files and optimizes the parameters of a constitutive relation based on a predefined target curve. The target curve was chosen as the

force-displacement curve from a typical tensile test in the rolling ($0°$) direction, and the FE model consisted of Belytschko-Tsay shell elements with an initial element size in the gauge area equal to the thickness of the specimens in an attempt to capture the local necking. Material constants for both materials based on LS-OPT are listed in Table 4, while physical constants taken from Holmen et al. [39][43] are provided in Table 5. The strain-rate sensitivity constant c for the 1050A-H14 aluminium alloy was taken from [44]. Comparisons between FE analyses and tensile tests are shown in Figure 3. Since necking occurred very early in the material tests, especially for the aluminium alloy, the results from the FE analyses are compared to the experimental data in terms of nominal stress-strain curves. It is seen that the numerical models are able to describe the overall response for both materials very well.

2.3. DIC measurements

Three-dimensional digital image correlation (3D-DIC) analyses were conducted for all blast tests using a stereovision setup with two Phantom v1610 high-speed cameras. The separation angle between the optical axes of the cameras was approximately 25° (Figure 1(a)). The recording rate was chosen to 21,000 fps in all tests with an image resolution of 896×800 pixels and 12-bit grey level digitization. The camera calibration and image analyses were carried out in a post-processing phase using an in-house finite element-based DIC code (see [45] for further details regarding the DIC software).

The calibration of the stereovision setup involved recordings of a calibration target with known geometry – in this case a cylinder with 80 mm diameter applied with a checkerboard pattern as shown in Figure 4(a). The calibration target was translated and rotated between each recording, and this process was done both prior to and in-between the blast tests to capture any potential permanent movement of the cameras during testing. The calibration target was initially pre-calibrated so that the dimensions, i.e., the diameter, square size and

possible deviations, of the cylinder were known with as high accuracy as possible. The location of the corners in the checkerboard pattern was extracted from the images (Figure 4(b)) and the 16 camera parameters including correction of radial and tangential lens distortion were optimized for each of the two cameras. The camera calibration and the 3D-DIC technique have been validated using shock-tube experiments and a laser displacement sensor (optoNCDT 2300) with similar experimental setup and sampling rate of data. The measured mid-point deflection based on the laser and the 3D-DIC were in excellent agreement, and the 3D-DIC technique is therefore considered as well suited to measure the displacements in this study.

Prior to each test, the plates were spray-painted with a speckle pattern. The thin plates were first spray-painted white before a template was used to apply black speckles with appropriate sizes on the white surface. The image sequences recorded during the blast loading tests were analysed using a finite-element formulation of DIC [45][46] on a mesh of Q4 elements. Zero-shifting and normalization of the grey values were carried out element-wise in the DIC analyses to handle large background light variations caused by the explosion.

Conversion between pixel locations in the images for the two cameras and the target space were carried out using the camera models presented in [45]. Figure 5 illustrates an example of recorded images from test S21 using the two synchronized high-speed cameras with the resulting DIC meshes plotted on top. The corresponding 3D model calculated from the DIC results is also illustrated in the figure.

Some challenges were encountered in the DIC analyses due to reflecting specular highlights, which occurred at various stages during the deformation of the plates. Also flaking of the paint, especially at the centre of the plates, were encountered in some of the tests. These challenges were however easily recognized, and the results from the DIC analyses at these locations were disregarded.

3. Experimental results

3.1. Pressure measurements

The measured blast-wave parameters from all tests against the rigid 15 mm thick steel plate are summarized in Table 6, while representative pressure-time histories for each stand-off distance are given in Figure 6. The pressure measurements were numbered RXY, where X denotes the subsequent stand-off distance (1, 2 and 3 – see Table 1) and Y is the test number. Since it is generally accepted that the structural response is mainly driven by the positive phase of the blast load [47][48], this study will merely focus on this phase. The reported blast-wave parameters are therefore limited to the time of arrival t_a, peak reflected overpressure $p_{r,\max}$, positive duration t_+ and impulse I_+ for typical pressure curves. These data were taken from the frame and the sensor where the blast wave arrived first, and the impulse was found by numerical integration of the pressure curve during the positive duration at the respective sensor. Measurements from the centre of the calibration plate (sensor 1) were also included in Table 6 for comparison. It should be noted that the blast parameters were not identical for the three pressure transducers in the frame at the same stand-off distance, but the sensor listed in Table 6 gives a good representation of these measurements from each test. All results were corrected according to the time of detonation using the signal from the break wire.

The pressure measurements show that the loading on the rigid calibration plate is in good agreement with the characteristics of an idealized blast wave, i.e., short rise time, exponential pressure decay and a positive phase followed by a negative phase. The variation in arrival time and peak reflected pressure for the blast wave at the respective sensors confirm that the pressure wave is spherical and propagates in a radial manner. This can be observed as the peak reflected pressure is decreasing and the time of arrival is increasing with increasing stand-off distance and oblique angle (Figure 6). This behaviour was further confirmed by the

difference in arrival time at the respective sensors, which became smaller at larger stand-off distances. It should also be noted that the sensors in the frame, i.e., 5-7 – see Figure 2 for the position of the various pressure transducers, were located about 30 mm closer to the charge than the sensors in the calibration plate (see Figure 1(a)). These sensors were included for a later comparison with the experiments involving the thin steel and aluminium plates.

For some reason the pressure seemed to arrive simultaneously at transducer 1 and 8 (see Figure 6) independent of stand-off distance. According to theory, it is expected that the blast wave would first arrive at transducer 1 and then the other sensors depending on their distance and oblique angle from the centre of the explosive charge. The same tendency was observed for the pressure recordings in the frame, where it was noticed that the pressure arrived somewhat earlier at sensor 6 compared to sensors 5 and 7. Since sensor 6 was on the same half of the calibration plate as sensor 8, these deviations may be explained by an imperfect shape and alignment of the explosive charge. However, since these deviations were relatively small it seems reasonable to assume a spherical shape and centred alignment in the following.

Other deviations worth noticing were the positive impulses from transducer 4 and 10 which were larger than expected compared to the other transducers. These somewhat irregular profiles are believed caused by a pressure build-up due to geometrical effects at the boundary, as the calibration plate was positioned differently than the clamping frame (Figure 1(a)). This was also confirmed by experimental and numerical investigations by Bonorchis and Nurick [49]. They showed that increased thickness of the clamping frame resulted in a pressure build-up at the plate boundary. However, this did not influence the mid-point deflection in subsequent experiments with deformable plates. It was also noted abnormal recordings in some sensors, e.g. sensor 7 in Figure 6(b) and sensor 9 in Figure 6(c), in some of the tests. The reason for this is not known.

Figure 7 shows that the pressure did not always return to the ambient pressure at the end of the experiments. This indicates that the reference value (or zero level) of the pressure transducers was altered during the experiment, which may be explained by the fact that the Kistler 603B transducers are only designed for temperatures up to $200\,°C$ [35]. It is therefore possible that the zero level changed due to the high temperature from the explosion, which seems reasonable since the drift was larger at the smallest stand-off distances where the temperature exposure was higher. This made it difficult to determine the exact duration of the negative phase. However, by assuming that the drift in pressure appeared after the positive phase, it was possible to determine the duration of the positive phase. This assumption seems reasonable since the fireball from the detonation is lagging behind the pressure wave. Reflection waves from e.g. secondary shocks and ground reflections were also observed in the pressure curves (seen as the peaks between 1 and 2 ms in Figure 7), making it even harder to determine the exact duration of the negative phase. Nevertheless, the overall performance of the pressure transducers seemed to be acceptable.

3.2. Steel plates

Figure 8 shows measured out-of-plane displacement at the centre point versus time for some of the tests based on the DIC analyses, while all experimental results are summarized in Table 7. The figure indicates that all plates experienced severe plastic deformation due to the blast load, and that the elastic rebound became smaller as the load-intensity increased. The specimens at the nearest stand-off distances of 125 mm and 250 mm (S11-S15 and S21-S23) experienced an intuitive response as the test specimen deformed in the same direction as the incident blast wave, before it started to oscillate around its final shape. However, the specimens at the largest stand-off distance of 375 mm (S31-S33) revealed a counter-intuitive response as the test specimen experienced reversed snap buckling during the elastic rebound,

before it started to oscillate around the final configuration in the opposite direction of the

incident blast wave. Due to trigger problems and flaking of the paint at the centre part in some

specimens, DIC analyses were only possible in 6 out of the 12 experiments conducted (see

Table 7). Further, the blast pencil recorded that the shock wave reached the cameras after

about 9 ms. Beyond this point the correlation of the images has reduced accuracy due to small

oscillations of the cameras. This is shown in Figure 8 as the non-physical deviation of the

displacement curves from the equilibrium configuration in the final part of the experiment.

As already mentioned, Table 7 gives characteristic blast parameters for a given pressure

sensor and the final out-of-plane displacement of the centre point from each test. The selected

data were taken from the sensor in the clamping frame (see Figure 2(b)) that first recorded

reasonable results. Thus, the variation in results observed at each stand-off distance represents

both the spread between the sensors and the natural spread in this type of tests. The final

displacement of the centre point measured with DIC ($d_{z,p1}$) and the in-situ permanent

displacement ($d_{z,p2}$) of the same point measured using a sliding caliper after the experiment

also reveal some differences. The DIC measurements, defined as the average displacement

during the elastic rebound phase, are in general slightly larger than the permanent

displacements. One reason for this may be that the plates were not necessarily completely at

rest when the final picture for the DIC analyses was taken.

Pictures of typical steel plates after blast loading are shown in Figure 9. For the closest

stand-off distance (Figure 9(a)), the deformed shape was square pyramidal with plastic hinges

around the boundaries and along the diagonals of the plate. Plastic hinges were also observed

for the two largest stand-off distances (Figure 9(b) and 9(c)), although not that distinct. In

these plates, a local dent at the centre with diameter similar to the spherical charge was

observed. Furthermore, there were no visible signs of tearing at the boundaries for the steel

plates and these experiments may therefore be classified as failure mode 1 [8], i.e., large

16

inelastic deformation. The only visible sign of failure in the test specimens was caused by some minor fragments from the detonator which had perforated the plate at the closest stand-off distance.

Figure 10 shows an example of synchronized loading and response histories during an experiment at the intermediate stand-off distance (from test S21). This figure also contains a selection of corresponding DIC images in terms of 3D topography maps, contours of the transverse displacement field and deformation profiles at characteristic times. It is observed from the synchronization of the pressure recordings and the DIC measurements that there was limited fluid-structure interactions (FSI) effects during the positive phase, since the positive duration of the pressure pulse was almost over before the plate started to move. Thus, subsequent motion took place during the negative phase and the structural response seemed to be driven mainly by the positive impulse from the airblast. The influence of the negative phase on the structural response seemed to be small until maximum deflection, as the shape of the displacement curve was barely altered during this phase. However, abnormal oscillations were observed subsequent to the elastic rebound (Figure 8). The synchronization of pressure and mid-point deflection in Figure 10 indicates that this unexpected behaviour may be due to the vacuum during the negative phase, i.e., the elastic rebound was enhanced by the negative phase. From the deformation profiles it is further observed that the maximum displacement had a small offset from the centre of the test specimen. This may stem from the positioning of the charge, which may have had an imperfect alignment relative to the centre of the plate. However, since the structural response seems to be driven by the imparted momentum, this offset may also stem from the boundary conditions or some other geometrical effect.

It was noted that the time of arrival t_a may be determined from the detonation pulse from the EBW detonator or taken from the calibration tests at the same stand-off distance, and the latter approach was used here. The former approach was only used at the closest stand-off

distance (S11-S15), as no calibration tests were performed at this configuration. The time of

arrival t_a for these tests was determined to be 0.07 ms. It should finally be stressed that the

pressure measurements in Table 7 must be treated with some caution, since the pressure

transducers were located at the clamping frame and not in the centre of the deforming plate.

Keep in mind that the pressure may change as the thin plates deform, and this is not captured

by these measurements. However, the limited FSI effects shown in Figure 10 and the pressure

measurements from Section 3.1 indicate that the pressure measured at the clamping frame

gives a good estimate of the loading on the plates.

3.3.   Aluminium plates

The aluminium plates showed in general similar dynamic structural response as the steel

specimens, but with some distinct differences. Figure 11 shows measured out-of-plane

displacement at the centre point versus time for some of the tests based on the DIC analyses,

while all results are summarized in Table 8. Compared to the steel specimens, it was observed

a larger variation in the test results and a wider range in structural response as the aluminium

specimens experienced both larger plastic deformations and failure (see Figure 12). It was

only possible to perform DIC analyses on 7 out of 9 experiments due to flaking of the paint at

the centre part in two of the tests. To reduce the risk of damaging the high-speed cameras it

was decided not to use DIC at the closest stand-off distance of 250 mm (A01), as the plate

was torn out of the clamping frame due to complete failure at the plate boundary (Figure

12(a)-12(c)). Due to the limited possibility to measure the structural response, it was chosen

to only perform one experiment at this stand-off distance. The failure mode observed at the

closest stand-off distance (A01) was similar to mode II as reported by e.g. [6][9][10], i.e.,

tensile tearing at the supports, while the tests at the subsequent stand-off distance of 375 mm

(A11-A13) experienced only partial tearing along the boundary (Figure 12(d)). The failure at

this stand-off distance was therefore classified as mode II*, in accordance with [8]. Thus, there was a transition between large inelastic deformations and complete tearing at the plate boundary. The failure was expected to start at the centre of the respective sides and propagate towards the corners with increasing impulse [8][10]. However, since the pressure sensors were located at these points in the clamping frame (Figure 12(c)), the clamping was locally reduced and fracture was first observed at the bolts closest to the centre of the plate boundary (Figure 12(d)). It was also observed a noticeably inward in-plane deflection at the centre of the plates for these experiments (Figure 12(c)-12(d)). This is sometimes called the "pulling-in" effect [8] and is a result of the plate deformation which continues between the time of first tearing at the boundary (mode II*) and complete tearing at the corners (mode II). As shown in Figure 12(d)-12(f) this effect seems to increase with increasing impulse as it was more evident at the closest stand-off distance. Before failure, "pulling-in" was not present and the plate experienced very limited sliding at the supports. As soon as failure occurred, there was a noticeably inward deflection at the centre of the plate. This resulted in some sliding at the supports and some deformation at the bolt holes, which is highlighted for the most evident case in Figure 12(c). The deformation was most severe at the holes closest to the pressure transducers due to the reduced clamping along the centre lines of the frame. Thus, it is possible that the "pulling-in" effect was enhanced by the reduced clamping at the centre lines of the plate, as experimental evidence (e.g. [10]) has shown a significant effect of the boundary conditions when predicting tearing.

The remaining two stand-off distances of 500 mm and 625 mm (A21-A23 and A31-A33) resulted in large inelastic deformation (mode I) and reversed snap buckling, respectively, as shown in Figure 12(e)-12(f). Synchronized loading and response histories from test A31, i.e., at the largest stand-off distance, can be found in Figure 13. In a similar way as for the steel plate in Figure 10, this figure contains a selection of DIC images in terms of 3D topography

maps, contours of the transverse displacement field and deformation profiles for characteristic times from the same test. Also these results revealed limited FSI effects during the positive phase as the duration of the positive part of the pressure pulse was almost over before the plate started to respond. Besides, the influence of the negative phase on the response up on maximum deformation seemed to be small since the shape of the displacement curve was barely altered during the negative phase. The selected DIC images for this particular test enabled a more detailed investigation of the reversed snap buckling phenomenon. Comparing Figure 8 and Figure 11, it is observed that the reversed snap buckling in the aluminium plates was somewhat different than in the steel plates, since the snap buckling did not occur during the elastic rebound. These plates experienced reversed snap buckling during the oscillations around its new equilibrium position, subsequent to the elastic rebound, and not during the rebound itself. This support previous observations by Symonds and Yu [14], which noted that the reversed snap buckling phenomenon is extremely sensitive to structural and loading parameters. The narrow range of structural and loading parameters related to this behaviour could be seen from the experiments at the intermediate stand-off distance (A21-A23 and S21-S23). Here abnormal oscillations subsequent to the elastic rebound were observed, indicating that these experiments were close to reversed snap buckling and that the transition between intuitive and counter-intuitive behaviour was between the two largest stand-off distances for both materials. Thus, a slight change in the intensity of the loading may result in a severe change in the structural response.

A closer look on Figure 11 shows a drop in the displacement curve starting at approximately 3 ms for all experiments with aluminium plates. This drop is more evident at increasing stand-off distances, which makes it reasonable to relate the reversed snap buckling in test A31-A33 to the duration of the negative phase. Unfortunately, the drift in the pressure measurements made it difficult to determine the duration of the negative phase and it is

challenging to conclude on the effect of the negative phase based on Figure 13. The influence

of the negative phase on the structural response therefore needs further investigations.

As for the steel plate experiments, the DIC analyses showed that the maximum response

was not always appearing at the centre of the plates (see Figure 13). However, the offset was

small in all tests. This may stem from the positioning of the charge, which may have had a

small offset from the centre of the plate. Since the deformation was driven by the impulse

from the airblast it is more likely to assume that the boundary conditions, or some other

geometrical effect, had a greater influence than the positioning of the charge on the deformed

shape. As the plate was given an initial velocity by the transferred impulse, the deformed

shape will be determined by the constraints at the boundary and the material properties.

The permanent deformation profile of the test specimens at the largest stand-off distance

revealed a local dent at the centre of the thin plate (see Figure 12(f)), similar to that in the

steel plate experiments. A closer examination of Figure 13(b)-13(c) indicates that the local

dent developed during the elastic rebound. This is also seen for the steel plate in Figure 10(b)-

10(c). Thus, as for the phenomenon of reversed snap buckling, it was observed that the

amount of plastic deformation determines the influence of the elastic rebound on the final

shape. That is, large deformations (as in e.g. A11) result in intuitively deformed shape

profiles, while smaller deformations reveal local dents at the centre and reversed snap

buckling (as in e.g. A31).

Since no calibration tests were performed at the largest stand-off distance (see Table 6),

the arrival time t_a for tests A31-A33 was determined using the detonation pulse from the

detonator. The shock wave produced by the EBW to detonate the charge of C-4 was seen on

the pressure measurements as an initial peak, and this was used as the best available estimate

for the time of detonation. By using this approach, the time of arrival for tests A31-A33 was

found to 0.56 ms.

21

It should also be noted that the duration of the positive phase was taken from the pressure sensors located on the clamping frame, and that this duration was found to be slightly less compared to the recordings on the calibration plate (Figure 6 and Table 6). Depending on the stand-off distance, the time of arrival is somewhat different at the calibration plate and the clamping frame. It was also observed that the end time of the positive phase was approximately the same at both locations. This implies that the pressure recordings in the clamping frame could be used as an estimate of the end time of the positive phase in the experiments. Despite this minor disagreement in pressure recordings, the loading was still defined as impulsive and the pressure measurements in the clamping frame were assumed reasonable to evaluate potential FSI effects. In a similar way as for the steel plates, the pressure measurements in Table 8 should be treated with some caution since the pressure may change as the plate deforms.

4. Concluding remarks

The influence of stand-off distance on the structural response of thin steel and aluminium plates subjected to airblast loading has been investigated experimentally. The loading was generated by detonating spherical charges of C-4 at various stand-off distances relative to the centre point of the plates, while the structural response was measured using two high-speed cameras in a stereovision setup combined with 3D-DIC analyses. The observations covered the entire range of structural response from complete ductile fracture at the supports to a more counter-intuitive behaviour in terms of reversed snap buckling at larger stand-off distances.

The overall trends in the experimental results were increased mid-point displacement of the plates and increased impulse transfer as the intensity of the blast-loading increased. This is shown in Figure 14 where the measured mid-point deflection-thickness ratio and scaled impulse as a function of scaled distance are plotted for all tests. Both the mid-point deflection

and the impulse seem to have a rather linear decrease with increasing stand-off distance. However, the impulse at the closest stand-off distance differs somewhat from this linear trend. This is probably due to reduced accuracy of the pressure sensors due to high temperatures, which is supported by the observation in Figure 9(a) where it is evident that the plate is slightly burned by the fireball at the closest stand-off distance. It is also noted that the plates experiencing reversed snap buckling deviates from the linear trend in Figure 14(a).

The increased mid-point displacement with increasing impulse is intuitive as long as the final deflection is in the same direction as the external load. This behaviour is also in accordance with the theory of impulsively loaded plates as discussed by Jones [50]. First, a phase with plastic hinges that starts at the boundary corners of the plate and propagates along the diagonals toward the centre is observed (see Figure 10(a) and Figure 13(a)). Then, when the plastic hinges meet in the centre of the plate (see Figure 10(b) and Figure 13(b)), a final phase develops with oscillations around a permanent deformed shape. However, the response at the largest stand-off distance for both materials was counter-intuitive as the plates experience reversed snap buckling and the final deflection of the plate was in the opposite direction of the incident blast wave.

The reversed snap buckling attracted special attention as it occurred both during and subsequent to the elastic rebound. The reversed snap buckling observed in Figure 8 during the elastic rebound is also observed in previous studies [12][13][21]. However, to the authors' best knowledge there are no previous experimental studies on metallic plates observing reversed snap buckling during the free vibrations around its new equilibrium position after the elastic rebound as shown in Figure 11. Based on the tests carried out, it is challenging to give an explanation of the observed phenomenon and also on how the negative phase of the load will influence the observed behaviour. The influence of the negative phase needs further investigations to determine the loading characteristics where this may dominate the response.

It is also interesting to note that the response of the steel and aluminium plates at the same stand-off distance of 375 mm (S31-S33 and A11-A13) results in a completely different final deformed shape, as the steel plates experience reversed snap buckling whereas the permanent displacement of the aluminium plates is in the intuitive direction.

The experiments also illustrate the possibilities of using finite element-based 3D-DIC for a thorough examination of the displacement field of structures exposed to fast transient loading. A comparison of the final deflections measured with DIC ($d_{z,p1}$) and the permanent displacement ($d_{z,p2}$) measured manually after the experiment (Table 7 and Table 8), indicated that there were some deviations in the two measurements. However, it should be emphasized that the DIC measurements are believed to be more accurate than the manually measured permanent displacement with the sliding caliper. The permanent displacement ($d_{z,p2}$) was included to indicate the accuracy in the DIC measurements, and to give experimental results when difficulties were observed with DIC. Thus, considering the potential sources of error in the manual measurements, DIC measurements should be used when available. The DIC technique also enabled a synchronization of the loading and response histories during the entire experiment, which provided new and accurate results under such extreme loading conditions.

This experimental study shows that thin ductile plates exposed to blast loading will experience large inelastic deformations, counter-intuitive response and possibly failure at the supports depending on the stand-off distance between the target and the explosive charge. Thus, depending on the characteristics of the blast load, the final deformed shape of the plate may become significantly different. This illustrates the importance of being able to capture such behaviour in computer-aided design of flexible protective structures. The numerical models must also be able to describe the influence of the elastic effects and the negative phase, which may play an important role in order to correctly predict the structural response.

It is therefore believed that the detailed experimental data reported in this study can be used in the development and evaluation of advanced computational methods often required for such problems. This will be investigated in full detail in a subsequent numerical paper [51].

Acknowledgement

References

[1] A. G. Hanssen, L. Enstock, M. Langseth, Close-range blast loading of aluminium foam panels, International Journal of Impact Engineering 2002;27:593-618.

[2] T. Børvik, A. G. Hanssen, S. Dey, H. Langberg, M. Langseth, On the ballistic and blast load response of a 20ft ISO container protected with aluminium panels filled with a local mass – Phase I: Design of protective system, Engineering Structures 2008;30:1605-1620.

[3] T. Børvik, A. Burbach, H. Langberg, M. Langseth, On the ballistic and blast load response of a 20ft ISO container protected with aluminium panels filled with a local mass – Phase II: Validation of protective system, Engineering Structures 2008;30:1621-1631.

[4] G. N. Nurick, J. B. Martin, Deformation of thin plates subjected to impulsive loading - A review - Part I – Theoretical considerations, International Journal of Impact Engineering 1989;8:159-170.

[5] G. N. Nurick, J. B. Martin, Deformation of thin plates subjected to impulsive loading - A review - Part II – Experimental results, International Journal of Impact Engineering 1989;8:171-186.

[6] S. B. Menkes, H. J. Opat, Broken beams – Tearing and shear failures in explosively loaded clamped beams, Experimental Mechanics 1973;13:480-486.

[7] R. G. Teeling-Smith, G. N. Nurick, The deformation and tearing of thin circular plates subjected to impulsive loads, International Journal of Impact Engineering 1991;11:77-91.

[8] M. D. Olson, G. N. Nurick, J. R. Fagnan, Deformation and rupture of blast loaded square plates – Predictions and experiments, International Journal of Impact Engineering 1993;13:279-291.

[9] G. N. Nurick, M. E. Gelman, N. S. Marshall, Tearing of blast loaded plates with clamped boundary conditions, International Journal of Impact Engineering 1996;18:803-827.

[10] G. N. Nurick, G. C. Shave, The deformation and tearing of thin square plates subjected to impulsive loads – An experimental study, International Journal of Impact Engineering 1996;18:99-116.

[11] T. Wierzbicki, G. N. Nurick, Large deformation of thin plates under localized impulsive loading, International Journal of Impact Engineering 1996;18:899-918.

[12] T. X. Yu, Chapter 9: Elastic effects in the dynamic plastic response of structures, Structural Crashworthiness and failure, In Proceedings of the Third International Symposium on Structural Crashworthiness, Edited by N. Jones and T. Wierzbicki, Taylor & Francis Ltd 1993:295-332.

[13] Q. M. Li, L. M. Zhao, G. T. Yang, Experimental results on the counter-intuitive behaviour of thin clamped beams subjected to projectile impact, International Journal of Impact Engineering 1991;11:341-348.

[14] P. S. Symonds, T. X. Yu, Counterintuitive behavior in a problem of elastic-plastic beam dynamics, ASME Journal of Applied Mechanics 1985;52:517-522.

[15] Q. M. Li, Y. M. Liu, G. W. Ma, The anomalous region of elastic-plastic beam dynamics, International Journal of Impact Engineering 2006;32:1357-1369.

[16] Q. M. Li, Y. M. Liu, Correlation between parameter sensitivity and counter-intuitive phenomenon of elastic-plastic beam dynamics, Computers & Structures 2006;84:156-165.

[17] G. Ma, Y. Liu, Q. M. Li, Numerical simulations of dynamic instability of elastic-plastic beams, Journal of Engineering Mechanics ASCE 2006;132:260-267.

[18] E. A. Flores-Johnson, Q. M. Li, A brief note on the counter-intuitive region of a square plate, International Journal of Impact Engineering 2011;38:136-138.

[19] P. S. Symonds, J. F. McNamara, F. Genna, Vibrations and permanent displacements of a pin ended beam deformed plastically by short pulse excitation, International Journal of Impact Engineering 1986;4:73-82.

[20] H. Kolosky, P. Rush, P. S. Symonds, Some experimental observations of anomalous response of fully clamped beams, International Journal of Impact Engineering 1991;11:445-456.

[21] S. U. Galiev, Experimental observations and discussion of counterintuitive behavior of plates and shallow shells subjected to blast loading, International Journal of Impact Engineering 1996;18:783-802.

[22] N. Jacob, S. Chung Kim Yuen, G. N. Nurick, D. Bonorchis, S. A. Desai, D. Tait, Scaling aspects of quadrangular plates subjected to localized blast loads – experiments and predictions, International Journal of Impact Engineering 2004;30:1179-1208.

[23] S. Chung Kim Yuen, G. N. Nurick, Experimental and numerical studies on the response of quadrangular stiffened plates. Part I: Subjected to uniform blast load, International Journal of Impact Engineering 2005;31:55-83.

[24] N. Jacob, G. N. Nurick, G. S. Langdon, The effect of stand-off distance on the failure of fully clamped circular mild steel plates subjected to blast loads, Engineering Structures 2007;29:2723-2736.

[25] A. Neuberger, S. Peles, D. Rittel, Springback of circular clamped armor steel plates subjected to spherical air-blast loading, International Journal of Impact Engineering 2009;36:53-60.

[26] B. Zakrisson, B. Wikman, H. Häggblad, Numerical simulations of blast loads and structural deformation from near-field explosions in air, International Journal of Impact Engineering 2011;38:597-612.

[27] K. Spranghers, I. Vasilakos, D. Lecompte, H. Sol, J. Vantomme, Full-field deformation measurements of aluminum plates under free air blast loading, Experimental Mechanics 2012;52:1371-1384.

[28] K. Spranghers, I. Vasilakos, D. Lecompte, H. Sol, J. Vantomme, Numerical simulation and experimental validation of the dynamic response of aluminum plates under free air explosions, International Journal of Impact Engineering 2013;54:83-95.

[29] L. Olovsson, A. G. Hanssen, T. Børvik, M. Langseth, A particle-based approach to close-range blast loading, European Journal of Mechanics A/Solids 2010;29:1-6.

[30] V. Tiwari, M. A. Sutton, S. R. McNeill, S. Xu, X. Deng, W. L. Fourney, D. Bretall, Application of 3D image correlation for full-field transient plate deformation measurements during blast loading, International Journal of Impact Engineering 2009;36:862-874.

[31] X. Zhao, V. Tiwari, M. A. Sutton, X. Deng, W. L. Fourney, U. Leiste, Scaling of the deformation histories for clamped circular plates subjected to blast loading by buried charges, International Journal of Impact Engineering 2013;54:31-50.

[32] M. A. Sutton, J.-J. Orteu, H. W. Schreier, Image correlation for shape, motion and deformation measurements, New York: Springer; 2009.

[33] G. Besnard, F. Hild, S. Roux, "Finite-element" displacement fields analysis from digital images: Application to Portevin-Le Châtelier Bands, Experimental Mechanics 2006;46:789-803.

[34] CEN, European Committee for Standardization, NS-EN 1090-2:2008+A1:2011, Execution of steel structures and aluminium structures - Part 2: Technical requirements for steel structures; 2008.

[35] Kistler Instrument Corp., Piezoelectric Pressure Sensor, Type 603B, http://www.kistler.com [cited 12.08.15].

[36] Swedish Steel AB (SSAB), Docol DP/DL Cold reduced dual phase steels, SSAB Swedish Steel Ltd, http://www.ssab.com [cited 12.08.15].

[37] G. Gruben, E. Fagerholt, O. S. Hopperstad, T. Børvik, Fracture characteristics of a cold-rolled dual-phase steel, European Journal of Mechanics A/Solids 2011;30:204-218.

[38] K. G. Rakvåg, N. J. Underwood, G. K. Schleyer, T. Børvik, O. S. Hopperstad, Transient pressure loading of clamped metallic plates with pre-formed holes, International Journal of Impact Engineering 2013;53:44-55.

[39] J. K. Holmen, O. S. Hopperstad, T. Børvik, Low velocity impact on multi-layered dual-phase steel plates, International Journal of Impact Engineering 2015;78:161-177.

[40] CEN, European Committee for Standardization, NS-EN 515 Aluminium and aluminium alloys – Wrought products – Temper designations; 1993.

[41] T. Børvik, O. S. Hopperstad, T. Berstad, M. Langseth, A computational model of viscoplasticity and ductile damage for impact and penetration, European Journal of Mechanics A/Solids 2001; 20: 685 – 712.

[42] Livermore Software Technology Corporation (LSTC), http://www.lstc.com [cited 06.11.15].

[43] J. K. Holmen, J. Johnsen, S. Jupp, O. S. Hopperstad, T. Børvik, Effects of heat treatment on the ballistic properties of AA6070 aluminium alloy, International Journal of Impact Engineering 2013; 57: 119 – 133.

[44] D. K. Christoulis, S. Guetta, V. Guipont, M. Jeandin, The influence of the substracte on the deposition of cold-sprayed titanium: An experimental and numerical study, Journal of Thermal Spray Technology 2011; 20: 523 – 533.

[45] E. Fagerholt, Field measurements in mechanical testing using close-range photogrammetry and digital image analysis. PhD-thesis, NTNU, Norway; 2012.

[46] E. Fagerholt, T. Børvik, O. S. Hopperstad, Measuring discontinuous displacement fields in cracked specimens using Digital Image Correlation with mesh adaptation and crack-path optimization, Optics and Lasers in Engineering 2013;51:299-310.
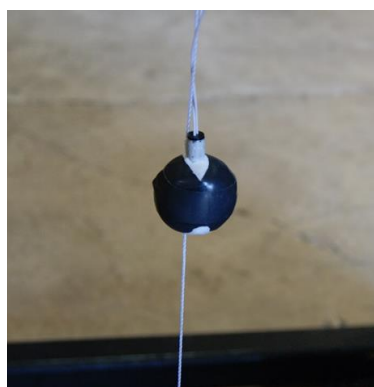
[47] Z. Xue, J. W. Hutchinson, Preliminary assessment of sandwich plates subjected to blast, International Journal of Mechanical Science 2003;45:687-705.

[48] X. Qiu, V. S. Deshpande, N. A. Fleck, Finite element analysis of the dynamic response of clamped sandwich beams subjected to shock loading, European Journal of Mechanics A/Solids 2003;22:801-814.

[49] D. Bonorchis, G. N. Nurick, The influence of boundary conditions on the loading of rectangular plates subjected to localised blast loading – Importance in numerical simulations, International Journal of Impact Engineering 2009;36:40-52.

[50] N. Jones, Structural Impact, Cambridge University Press, Second Edition; 2012.

[51] V. Aune, G. Valsamos, F. Casadei, M. Langseth and T. Børvik. The influence of elastic effects and negative phase on the structural response of blast-loaded thin aluminium and steel plates, To be submitted for possible journal publication, 2016.
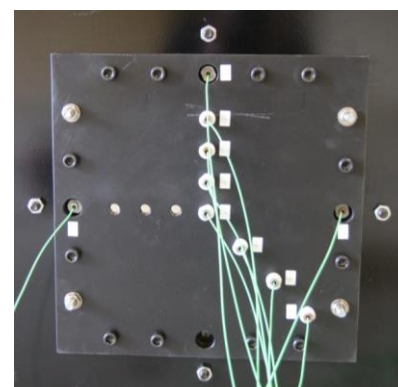
(a) Sketch of setup
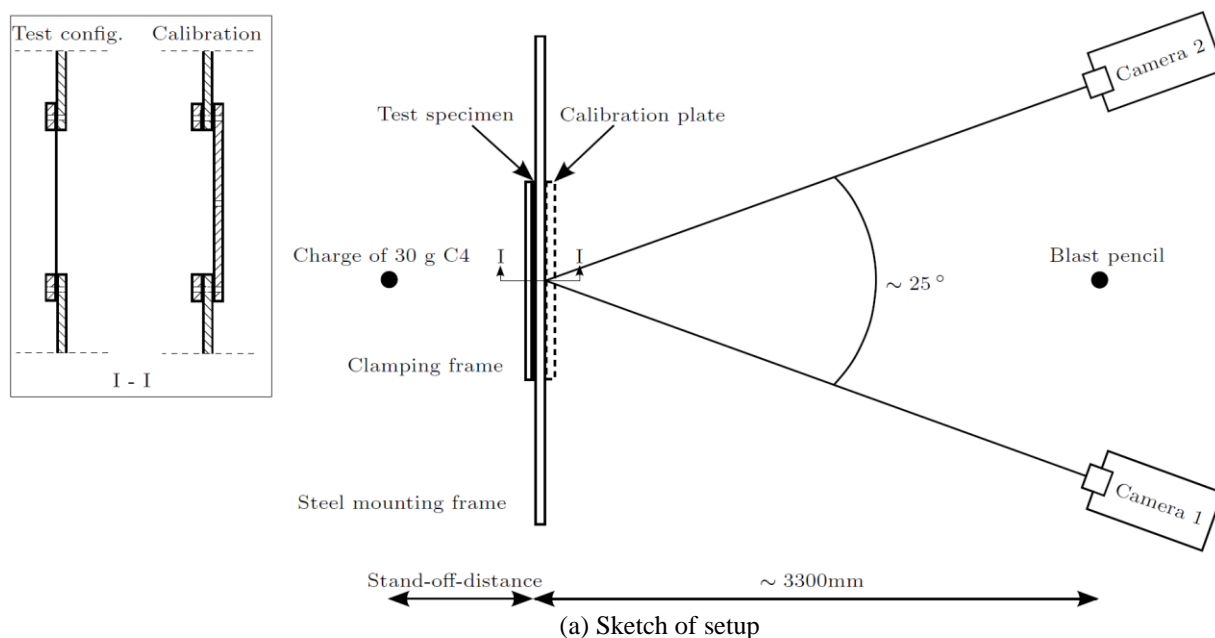
(b) Picture of setup
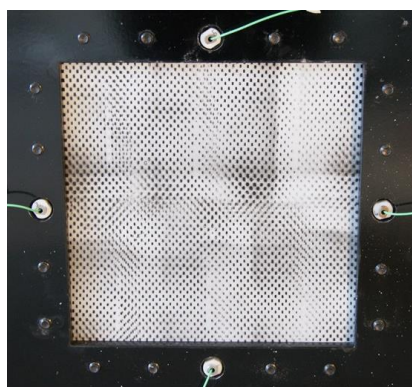
(c) DIC speckle pattern   (d) Spherical charge   (e) Calibration plate

Figure 1. Experimental setup. Both the speckle pattern in (c) and the calibration plate in (e) are seen from the cameras.

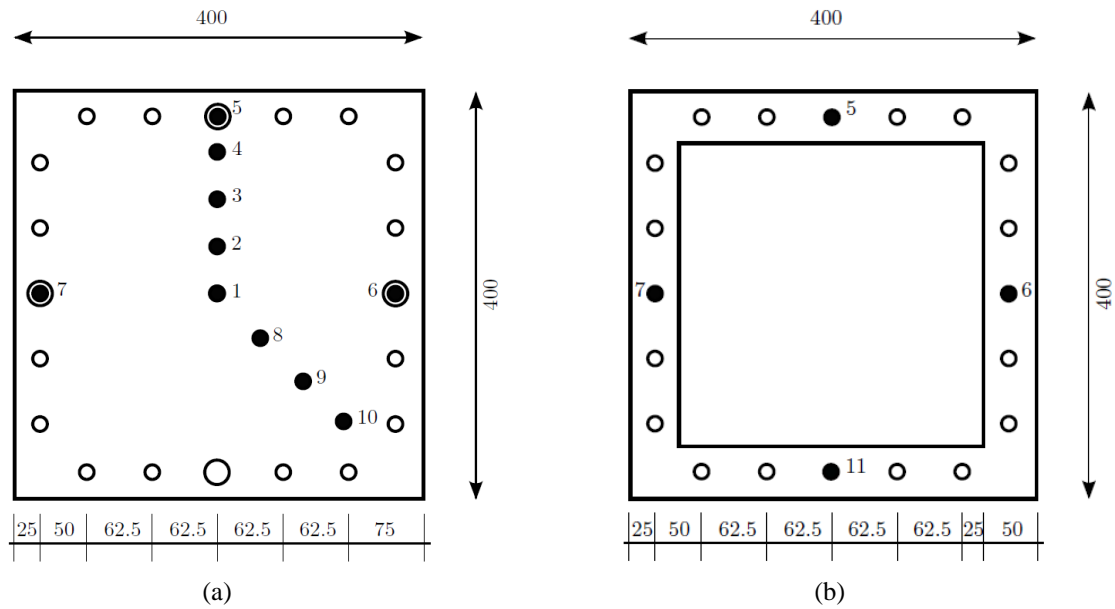Figure 2. Position of pressure transducers (seen from the cameras) in the calibration plate (a) and clamping frame (b). All measurements are in mm.
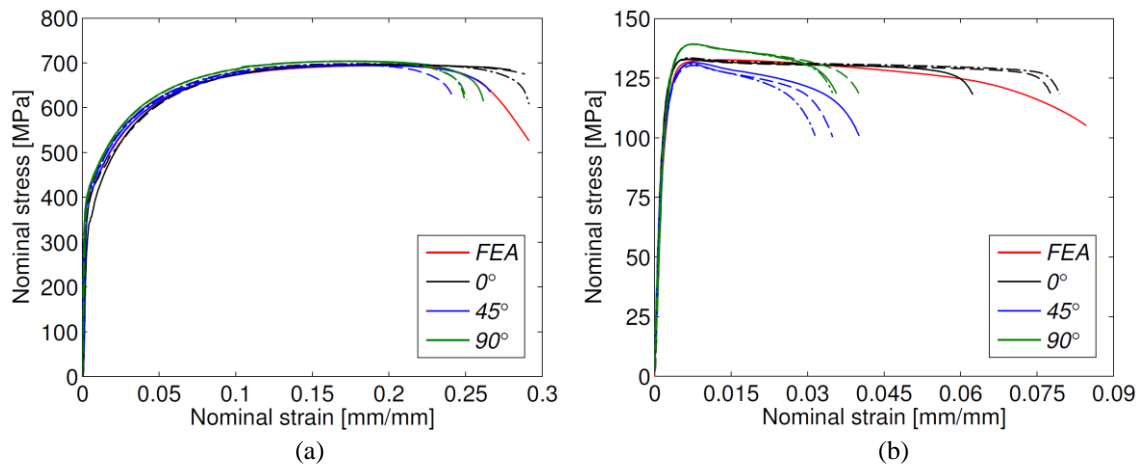

Figure 3. Nominal stress-strain curves from uniaxial tensile tests at three different loading directions for (a) Docol 600DL [39] and (b) EN AW 1050A-H14. Numerical results from LS-DYNA simulations with material data from Table 4 and Table 5 are included for comparison.

33

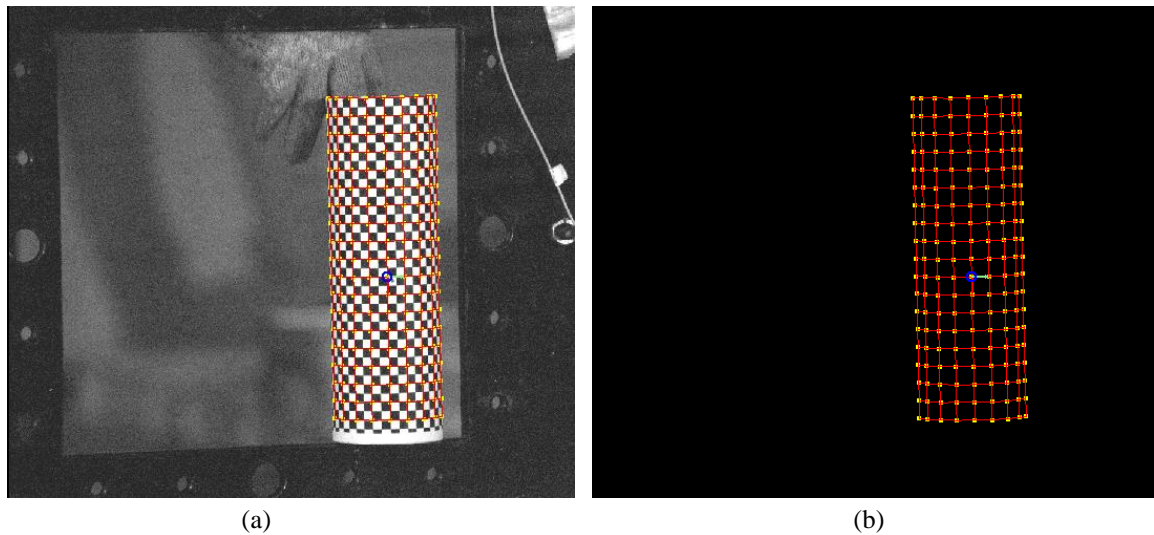(a)   (b)

Figure 4. Calibration of the stereovision setup. (a) A recorded image of the calibration target (cylinder) is analysed to find the corners of the checkerboard pattern. (b) The extracted corner positions in the image (pixels) and in the three-dimensional target coordinate system (mm) is used to calibrate the 16-parameter camera models [45]. Multiple recordings of the calibration target are used to obtain trustworthy camera models.
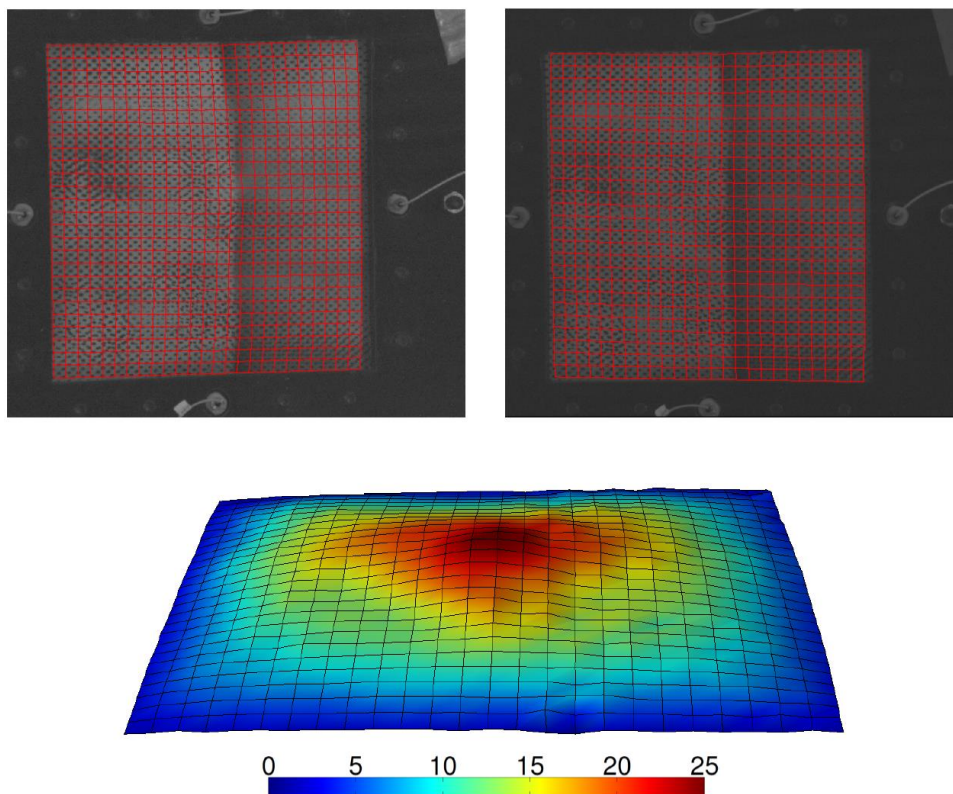
Figure 5. Results from 3D-DIC from test S21. The top images show two corresponded images from camera 1 (top-left) and camera 2 (top-right). The resulting DIC mesh is plotted on-top of the recorded images. The corresponding 3D model from DIC is presented in the lower image. The colour scaling on the 3D-model indicates out-plane displacement (in mm).

a) R13 - vertical (left), diagonal (middle) and frame (right)

b) R23 - vertical (left), diagonal (middle) and frame (right)

c) R33 - vertical (left), diagonal (middle) and frame (right)
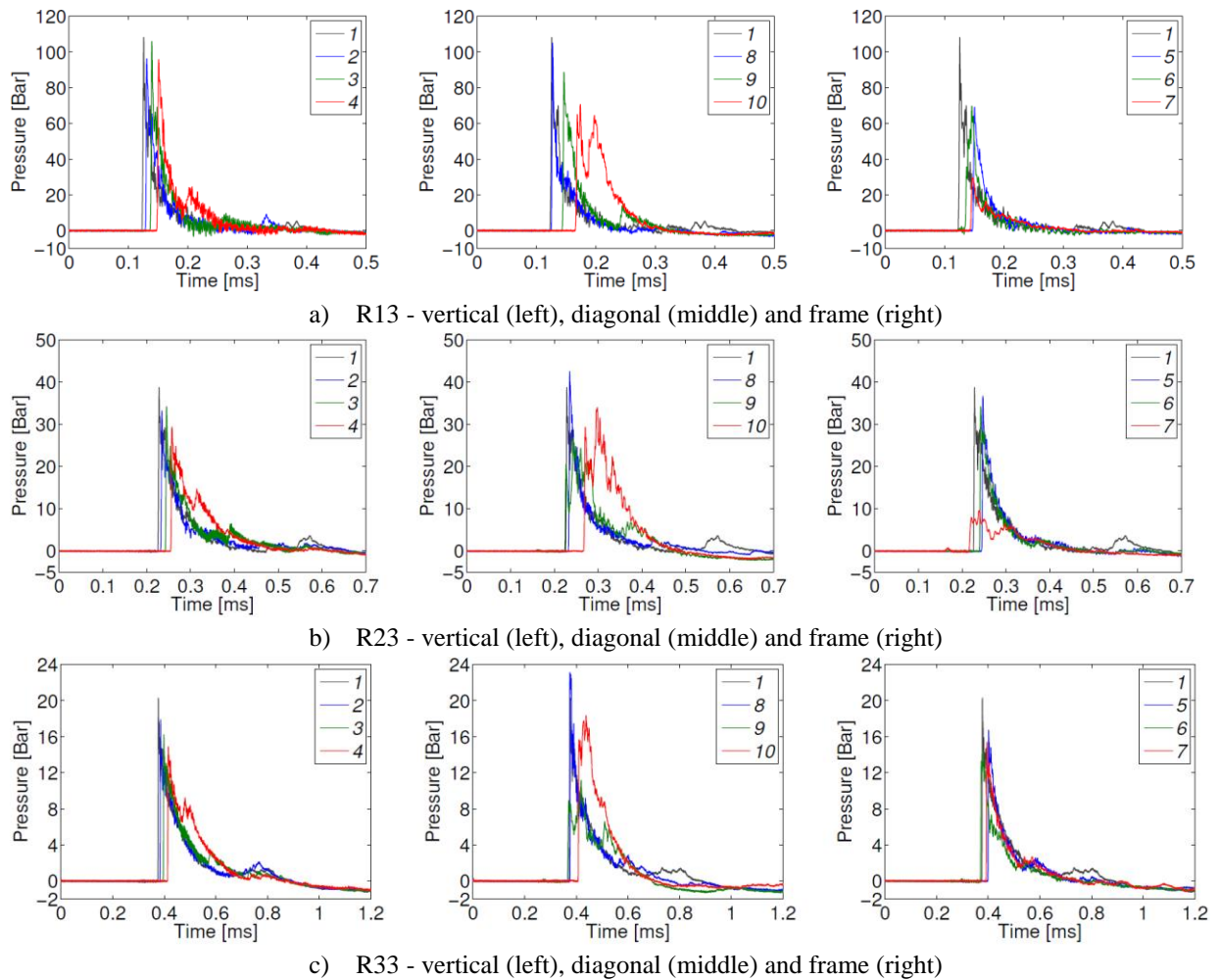
Figure 6. Pressure measurements from selected experiments restricted to only include the positive phase of the blast load. See Figure 2 for the location of the pressure transducers.

Figure 7. Secondary reflections and pressure drift in pressure transducers from test R33.
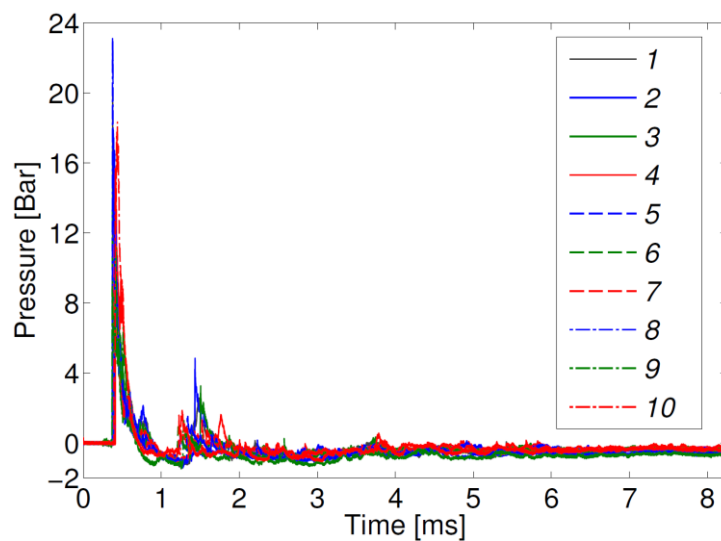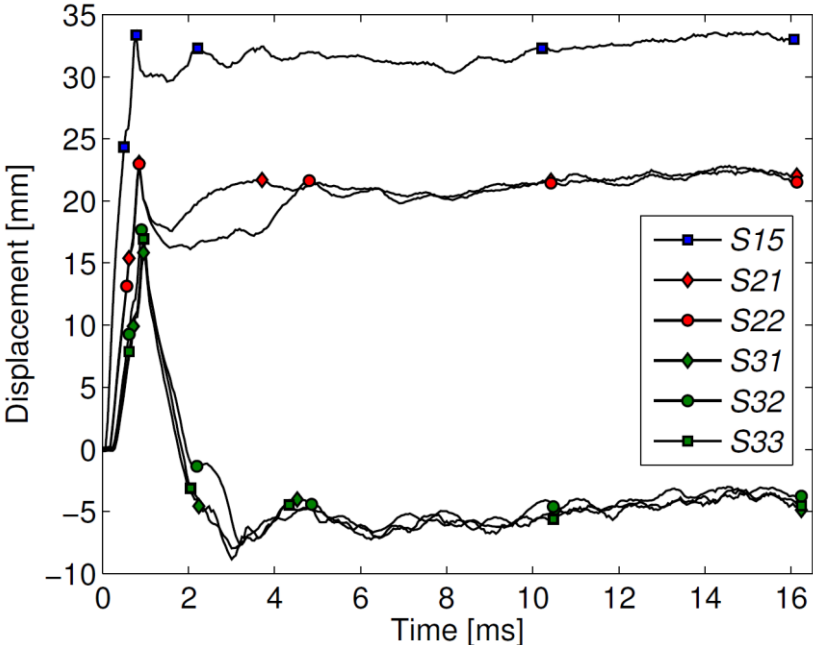
Figure 8. Deformation versus time of the centre point for the steel plates based on 3D-DIC.

(a) S15   (b) S22   (c) S33
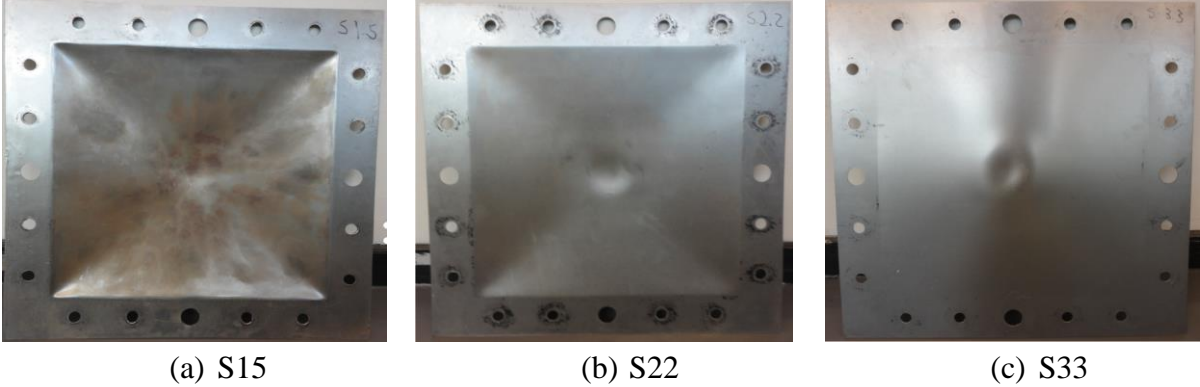
Figure 9. Photographs of deformed shapes for selected steel plates (seen from the explosive charge).

(a) t = 0.612 ms

(b) t = 0.850 ms

(c) t = 1.326 ms

(d) t = 1.565 ms

(e) t = 3.707 ms

Figure 10. A selection of DIC images from test S21 with 3D topography maps and contours of the transverse displacement (left), its corresponding pressure and centre deformation (middle) and deformation profile at centre along x-axis (right). Pressure recordings from sensor 11 are used in the synchronization. Red squares show the corresponding time of recordings.
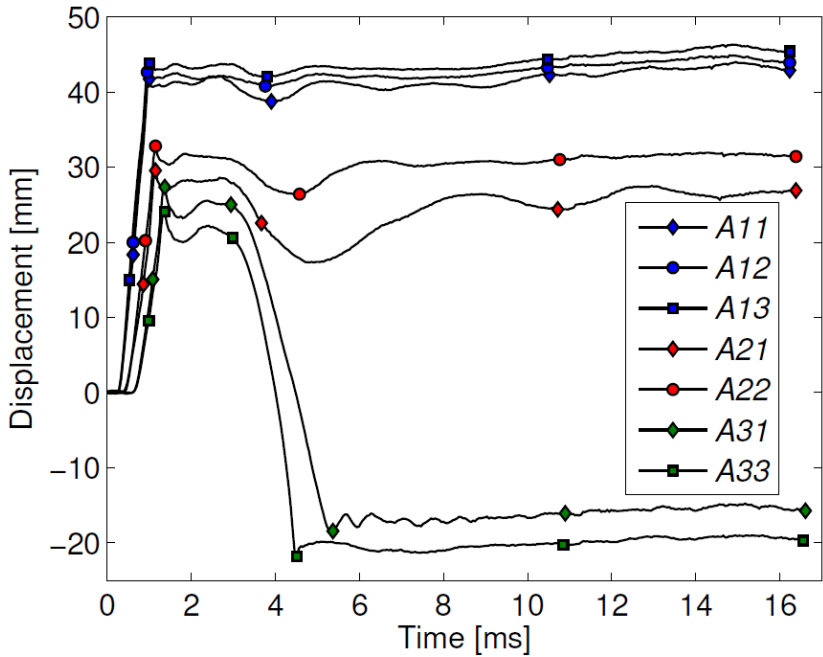
Figure 11. Deformation versus time of the centre point for the aluminium plates based on 3D-DIC.

(a) A01	(b) A01	(c) A01
(d) A11	(e) A22	(f) A33
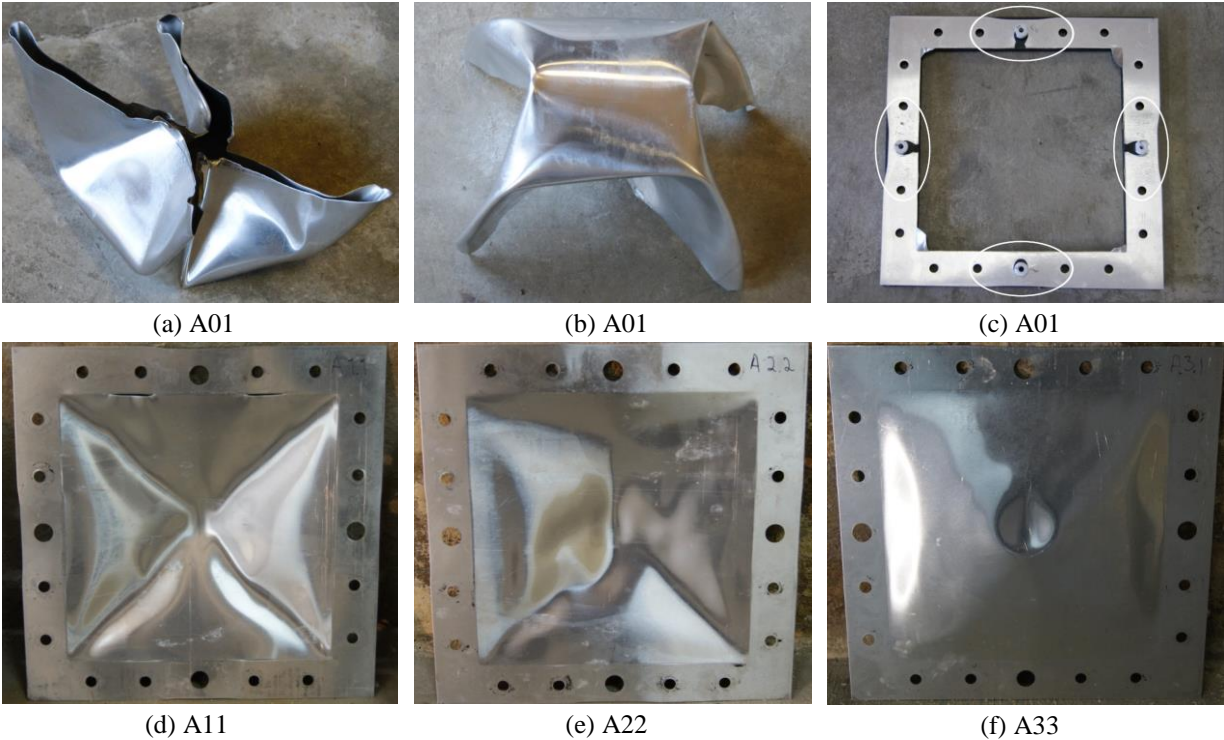
Figure 12. Photographs of deformed shapes for selected aluminium plates. All pictures are seen from the explosive charge except for (b).

(a)   t = 1.087 ms

(b)   t = 1.372 ms

(c)   t = 1.753 ms

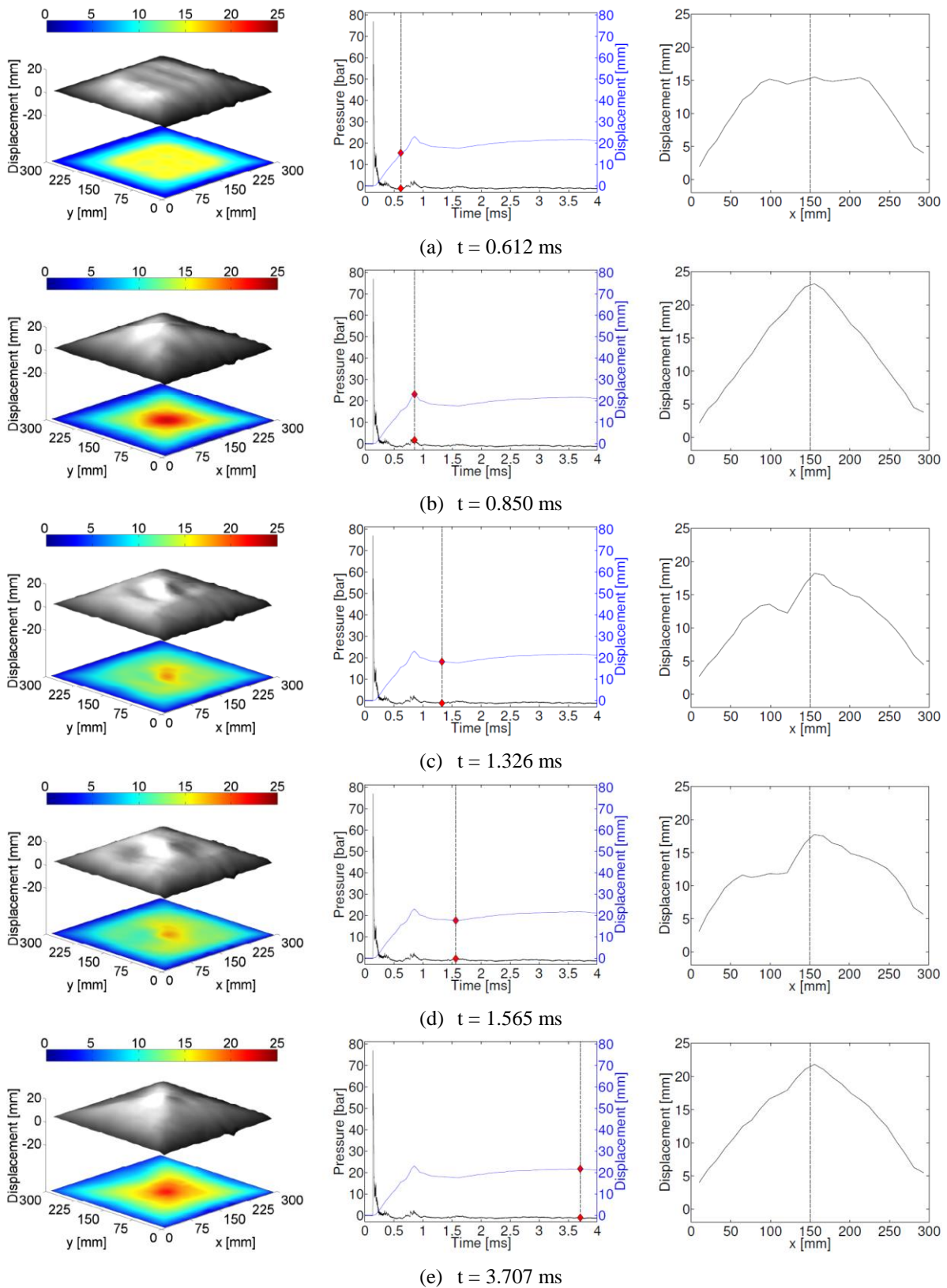(d)   t = 3.658 ms

(e)   t = 5.372 ms
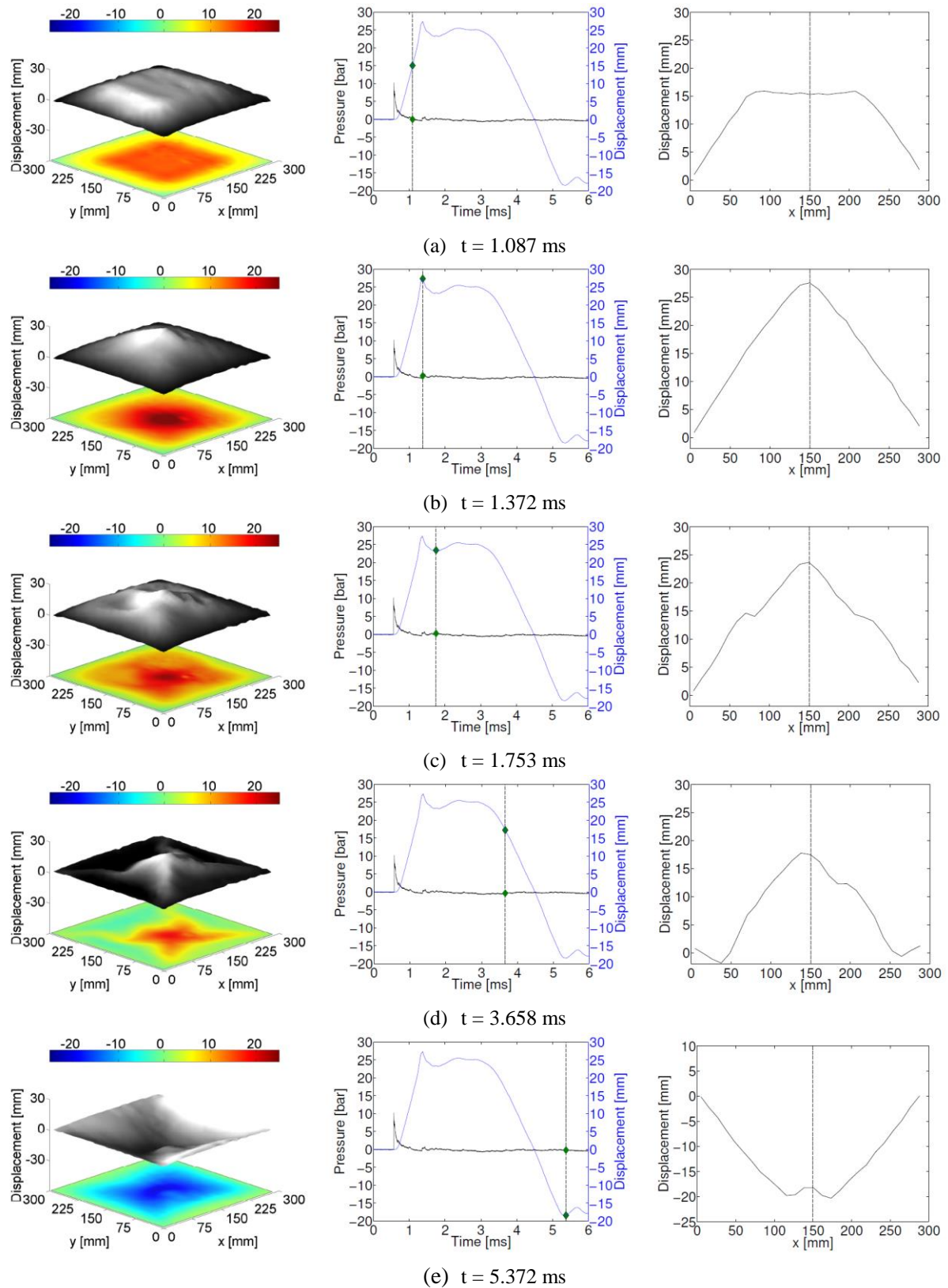
Figure 13. A selection of DIC images from test A31 with 3D topography maps and contours of the transverse displacement (left), its corresponding pressure centre deformation (middle) and deformation profile at centre along x-axis (right). Pressure recordings from sensor 6 are used in the synchronization. Green squares show the corresponding time of recordings.

Figure 14. Measured mid-point deflection-thickness ratio (a) and scaled impulse from a selected sensor in the frame (b) versus scaled distance. In (a) the open symbols are from the 3D-DIC measurements, while the closed symbols are from the manual measurements using a slide caliper.

Table 1. Test matrix.

Plate thickness [mm]	Stand-off distance, R [m]	Test number 1	2	3	4	5
15 (rigid steel plate)	0.250	R11	R12	R13	-	-
	0.375	R21	R22	R23	-	-
	0.500	R31	R32	R33	-	-
0.8 (steel plate)	0.125	S11	S12	S13	S14	S15
	0.250	S21	S22	S23	-	-
	0.375	S31	S32	S33	-	-
0.8 (aluminium plate)	0.250	A01	-	-	-	-
	0.375	A11	A12	A13	-	-
	0.500	A21	A22	A23	-	-
	0.625	A31	A32	A33	-	-

Table 2. Chemical composition of Docol 600DL (in wt.%).

C	Si	Mn	P	S	Al
0.10	0.40	1.50	0.010	0.002	0.040

Table 3. Chemical composition of EN AW 1050A-H14 (in wt.%).

Si	Fe	Cu	Mn	Mg	Zn	Ti	Al
0.030	0.360	0.001	0.002	0.000	0.003	0.010	Rest

Table 4. Material parameters for the modified Johnson-Cook (MJC) constitutive relation.
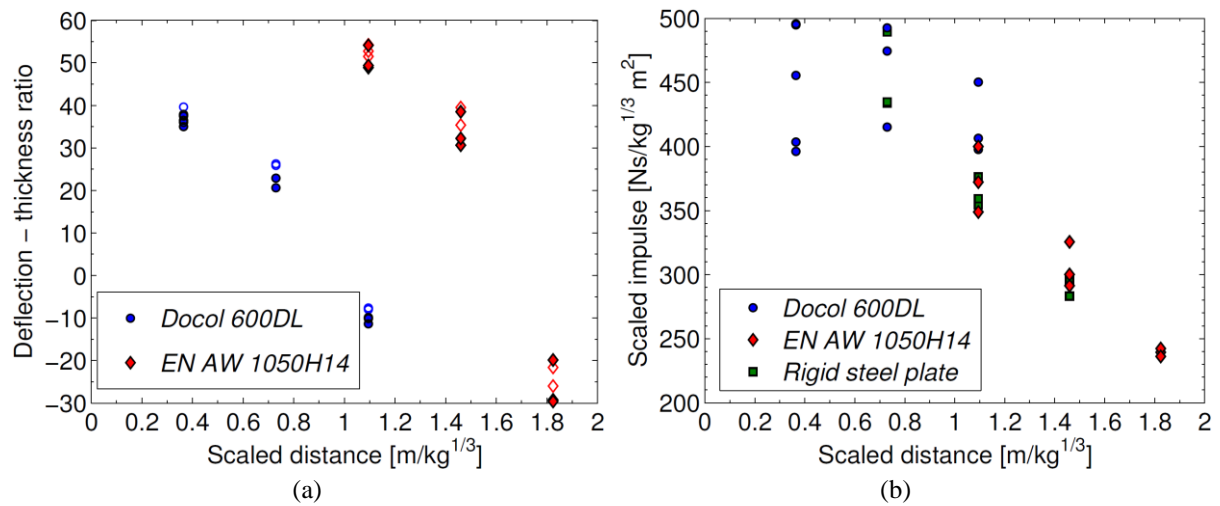
Material	σ_0 [MPa]	Q_1 [MPa]	C_1 [-]	Q_2 [MPa]	C_2 [-]	c [-]	m [-]	$\dot{p}_0$ [s^{-1}]
Docol 600DL [39]	370.0	236.4	39.3	408.1	4.5	0.001	1.0	5×10^{-4}
1050A-H14	80.0	49.3	1457.1	5.2	121.5	0.014	1.0	5×10^{-4}

Table 5. Physical constants for the materials taken from the litterature.

Material	E [GPa]	ν [MPa]	ρ [kg/m^3]	α [K^{-1}]	C_p [J/kgK]	χ [-]	T_r [K]	T_m [K]
Docol 600DL [39]	210.0	0.33	7850	1.2×10^{-5}	452	0.9	293	1800
1050A-H14 [43]	70.0	0.30	2700	2.3×10^{-5}	910	0.9	293	893

Table 6. Experimental results from pressure measurements. The location of the pressure transducers are given in Figure 2.

Test	R [m]	$Z = R/W^{1/3}$ [m/kg$^{1/3}$]	Sensor [#]	t_a [ms]	$p_{r,\max}$ [bar]	t_+ [ms]	I_+ [Ns/m^2]
R11	0.235	0.69	7	0.12	82.5	0.18	148.6
	0.265	0.77	1	0.10	55.2	0.15	189.8
R12	0.235	0.69	7	0.14	68.8	0.16	148.9
	0.265	0.77	1	0.11	204.3	0.18	303.0
R13	0.235	0.69	6	0.13	69.7	0.15	167.6
	0.265	0.77	1	0.12	108.1	0.17	207.2
R21	0.360	1.05	7	-	32.6	0.22	121.4
	0.390	1.14	1	-	47.8	0.23	168.1
R22	0.360	1.05	5	-	36.2	0.25	123.1
	0.390	1.14	1	-	46.0	0.22	167.7
R23	0.360	1.05	6	0.25	34.2	0.25	128.9
	0.390	1.14	1	0.23	38.8	0.23	151.2
R31	0.485	1.42	6	0.38	17.2	0.39	101.2
	0.515	1.50	1	0.39	18.5	0.51	143.5
R32	0.485	1.42	5	0.40	16.3	0.38	97.0
	0.515	1.50	1	0.39	11.6	0.51	95.6
R33	0.485	1.42	6	0.37	14.5	0.38	101.3
	0.515	1.50	1	0.37	20.3	0.51	144.9

Table 7. Experimental results for the steel plates.

Test	R [m]	$Z = R/W^{1/3}$ [m/kg$^{1/3}$]	Sensor[*] [#]	$p_{r,max}$ [bar]	t_+ [ms]	I_+ [Ns/m^2]	t_+/T_n [-]	$d_{z,p1}$ [mm]	$d_{z,p2}$ [mm]	DIC [Y/N]
S11	0.125	0.36	11	142.0	0.07	135.7	0.005	-	30.0	N
S12	0.125	0.36	11	145.5	0.07	169.5	0.005	-	29.2	N
S13	0.125	0.36	11	162.0	0.07	156.0	0.005	-	28.8	N
S14	0.125	0.36	11	149.1	0.07	169.8	0.005	-	30.3	N
S15	0.125	0.36	11	115.1	0.07	138.2	0.005	31.7	28.0	Y
S21	0.250	0.73	11	76.9	0.17	162.5	0.013	20.7	16.5	Y
S22	0.250	0.73	6	67.6	0.14	142.2	0.011	21.0	18.3	Y
S23	0.250	0.73	7	76.7	0.14	168.7	0.011	-	18.3	N
S31	0.375	1.09	11	34.9	0.25	139.2	0.019	-6.4	-8.1	Y
S32	0.375	1.09	6	49.2	0.23	154.2	0.017	-6.1	-7.9	Y
S33	0.375	1.09	6	32.9	0.21	136.2	0.016	-6.2	-9.1	Y

[*]Stand-off distance R refers to the respective plate, and not to the sensor located in the frame.

Table 8. Experimental results for the aluminium plates.

Test	R [m]	$Z = R/W^{1/3}$ [m/kg$^{1/3}$]	Sensor[*] [#]	$p_{r,max}$ [bar]	t_+ [ms]	I_+ [Ns/m^2]	t_+/T_n [-]	$d_{z,p1}$ [mm]	$d_{z,p2}$ [mm]	DIC [Y/N]
A01	0.250	0.73	6	98.0	0.11	185.7	0.008	-	-	N
A11	0.375	1.09	6	30.8	0.22	119.5	0.016	41.2	39.1	Y
A12	0.375	1.09	7	38.0	0.18	127.5	0.013	42.2	39.5	Y
A13	0.375	1.09	11	42.8	0.23	137.0	0.017	43.4	43.3	Y
A21	0.500	1.46	11	17.1	0.40	111.5	0.030	28.3	24.5	Y
A22	0.500	1.46	7	15.2	0.35	99.8	0.026	31.6	30.8	Y
A23	0.500	1.46	7	15.3	0.36	102.8	0.026	-	25.8	N
A31	0.625	1.82	6	10.2	0.54	82.0	0.040	-17.3	-15.9	Y
A32	0.625	1.82	11	9.3	0.48	83.0	0.036	-	-23.4	N
A33	0.625	1.82	6	7.9	0.54	80.9	0.040	-20.8	-23.7	Y

[*]Stand-off distance R refers to the respective plate, and not to the sensor located in the frame.